



Hindcasting nearshore wind waves using a FEM code for SWAN

Tai-Wen Hsu*, Shan-Hwei Ou, Jian-Ming Liao

Department of Hydraulic and Ocean Engineering, National Cheng Kung University, Tainan 701, Taiwan

Received 23 April 2004; received in revised form 18 October 2004; accepted 11 November 2004

Available online 18 January 2005

Abstract

An improved SWAN model using the Finite Element Method (FEM) was developed for wind waves simulations in both large-scale oceanic deep water regions and small-scale shallow water regions. The model employs a Taylor–Galerkin finite element technique for the discretization of the modeled area, which makes it flexible to represent bottom topography and irregular boundaries. The fractional step numerical scheme was adopted to split the wave action balance equation into three one-dimensional space equations, which can be solved efficiently by one-dimensional algorithms. The Flux-Corrected Transport method was also applied to circumvent the steep-gradients of the action density in the frequency space. The FEM code with unstructured grids improves the numerical schemes in the original SWAN to maintain computational efficiency at the operational stage. A simulation of wind wave activities for the monsoon and the 2000 Typhoon Bilis were performed using the FEM and SWAN models. The simulated results were compared with field observations in order to verify the suitability of the method.

© 2004 Elsevier B.V. All rights reserved.

Keywords: Wind waves; SWAN; Finite Element Method; Fractional step method; Flux-Corrected Transport algorithm

1. Introduction

Many coastal and offshore engineering applications require detailed knowledge of wave conditions at specific locations. Usually, such information is not available, due to incomplete (or in absence of) observational records. In such cases, predictions of the wave conditions by numerical models become a popular tool, as they may provide the good estimate of

the environmental conditions at a location for given wind fields.

WAM (acronym for Wave Model) and SWAN (acronym for Simulating Wave Nearshore) are third-generation wave models used to compute spectra of random short-crested waves in coastal waters. The WAM code has been primarily developed by the WAMDI Group (1988) to generate wave predictions in oceanic basins and deep water regions, whereas the SWAN code has been developed by Booij et al. (1999) and validated specially in coastal regions with shallow water, islands (barrier), tidal flats, local wind, and ambient currents. The WAM code is suitable to

* Corresponding author. Tel.: +886 6 2372315; fax: +886 6 2741463.

E-mail address: twhsu@mail.ncku.edu.tw (T.-W. Hsu).

account for deep water ocean waves which are mainly wind-driven, while the SWAN code is applicable to present nearshore wave propagation processes such as shoaling, refraction, and wave breaking due to finite-depth effect. The quadruplet wave–wave interactions which dominate the wave spectrum evolution in deep water are used for the WAM model, whereas the triad wave–wave interactions which are important in shallow water are used for the SWAN model.

In SWAN, the evolution of wave spectrum is described by the action balance equation rather than the energy transport equation, because the wave action density spectrum is conserved in the presence of currents, but the energy density spectrum is not. SWAN solves the integration of the action balance equation using a fully implicit upwind scheme in geographic space. The rectangular grids are implemented in the finite-difference scheme in SWAN. However, the use of equal space grids for the case of complex geometries of general coastal environments together with the rapid change of bottom configurations may make SWAN problematic and inefficient. Typically, a uniform grid used in SWAN for an entire domain from deep water to shallow water could result in over-resolved in the offshore region and under-resolved in the nearshore zone. To resolve the evolution of a broad spectrum of wind waves, SWAN uses a fine spatial discretization in shallow water areas that becomes expensive for large coastal zones.

To overcome the increased computational demands of SWAN for nearshore applications where complex bathymetry and irregular shoreline often require a fine resolution, the nested grid system is used. More recently the upgraded SWAN model of version 40.11 has been developed by [Holthuijsen et al. \(2000\)](#) to provide an option for coupling a coarse-nest WAM and a fine-nest SWAN simulation for nearshore wave predictions. The entire domain is generally divided into some subregions with varying spatial grid sizes according to the desired resolution. A WAM/SWAN interface is also specified to allow the stationary boundary conditions for a fine-nest SWAN simulation provided by a coarse-nest WAM simulation. [Wornom et al. \(2001\)](#) performed a numerical test using a simulation of wind–wave activity for the 1995 Hurricane Luis, and found that the SWAN code in the finest WAM nest can be an effective means of combining the deep water and shallow water strengths

of the two codes to result in more accurate nearshore wave estimates.

For numerical models, the computational efficiency and reliability are the most important factors for realistic applications. Although the implicit scheme is employed in SWAN to permit relatively large time-step to avoid numerical instabilities and to save computer time, a large time-step may increase numerical dispersion and dissipation errors as demonstrated by [Rogers et al. \(2002\)](#). This implies that the time-step has to be reduced for a fine-nest to capture unsteady physical features rather than to maintain numerical stability, but this required time-step will increase the computer time. Moreover, the computational procedures in coupling the WAM and SWAN interface through the boundary spectra, that were provided by a WAM or SWAN run, may lead to a heavy management of input/output files, complicated programming, and significant increase in computational effort. Hence, it is necessary to find better numerical schemes capable of overcoming this challenge in shallow water area.

The Finite Element Method (FEM) has the advantage to display more accurately complicated bathymetry and irregular boundaries for shallow water areas. It can also solve the combined large-scale oceanic and small-scale coastal waves in the same discrete domain by using the unstructured meshes. The finite element technique overcomes the nested grid problem mentioned above, because the local size of the mesh and number of nodes can be optimized in the various parts of the computational domain. The coastal waters areas are discretized with triangular elements, whose sizes are varied according to the desired resolution. This feature allows the flexibility to have a coarse mesh on a large-scale area and a fine mesh on a small-scale area. The aim of this paper is to present a FEM code for the SWAN model. The original SWAN's nested grid scheme is improved to offer a more efficient wave prediction model for small-scale, shallow water regions. Typical tested cases used for verification are the waves propagating from deep water to the nearshore coastal regions of Taiwan, which are generated by the monsoon wind and typhoon, respectively. Comparisons of the model results with actual wave measurements provide the evaluation of the computational economy and applicability of the original SWAN and the FEM codes.

2. The action balance equation

In SWAN, the evolution of the wave spectrum is described by the spectral action balance equation, which is expressed by Cartesian coordinates as follows (e.g., Hasselmann et al., 1973).

$$\begin{aligned} \frac{\partial}{\partial t}N + \frac{\partial}{\partial x}(C_x N) + \frac{\partial}{\partial y}(C_y N) + \frac{\partial}{\partial \sigma}(C_\sigma N) \\ + \frac{\partial}{\partial \theta}(C_\theta N) = S_{\text{total}} \end{aligned} \quad (1)$$

where $N=N(t,x,y,\sigma,\theta)$ is the wave action density spectrum; t is the time; C_x and C_y are the wave propagation velocities in x and y space, respectively; C_σ and C_θ are the wave propagation velocities in σ and θ space, respectively; σ is the relative frequency; θ is the wave direction; $S_{\text{total}}=\tilde{S}_{\text{total}}(\sigma,\theta)/\sigma$ is the source term; and \tilde{S}_{total} is the spectral density of wave energy. The first term on the left-hand side of Eq. (1) represents the time rate of change of the action density. The second and third term represent propagation of the action density in the geographical space. The fourth term represents shifting of the relative frequency due to variations in the depth and the current. The fifth term represents the refraction induced by variations in the depth and the current. The term at the right-hand side is the source term in terms of the energy density, representing the combined effects of wave generation, dissipation, and nonlinear wave–wave interactions.

For applications on large-scale oceanic regions, the action balance equation, Eq. (1), needs to be reformulated in terms of the spherical coordinates. The longitude–latitude formulation of the action balance equation is given by

$$\begin{aligned} \frac{\partial \hat{N}}{\partial t} + (\cos\phi)^{-1} \frac{\partial}{\partial \phi} (\dot{\phi} \cos\phi \hat{N}) + \frac{\partial}{\partial \lambda} (\dot{\lambda} \hat{N}) \\ + \frac{\partial}{\partial \sigma} (\dot{\sigma} \hat{N}) + \frac{\partial}{\partial \theta} (\dot{\theta} \hat{N}) = S_{\text{total}} \end{aligned} \quad (2)$$

where $\hat{N}=\hat{N}(\phi,\lambda,\sigma,\theta,t)$ is the wave action density spectrum for spherical coordinates; ϕ is the latitude; λ is the longitude; $\dot{\phi}$ is the time rate of change of ϕ ; $\dot{\lambda}$ is the time rate of change of λ ; $\dot{\sigma}$ is the time rate of

change of the relative frequency; and $\dot{\theta}$ is the time rate of change of the propagation direction.

The wave action density spectrum \hat{N} is related to the normal spectral density N with respect to a local Cartesian coordinates through $\hat{N}d\sigma d\theta d\phi d\lambda = Nd\sigma d\theta dx dy$, or

$$\hat{N} = NR^2 \cos\phi \quad (3)$$

where R is the radius of the earth. The expressions of $\dot{\phi}$, $\dot{\lambda}$, $\dot{\sigma}$, and $\dot{\theta}$ are given, respectively, by

$$\dot{\phi} = (C_g \cos\theta + \mathbf{U}/\text{north})R^{-1} \quad (4a)$$

$$\dot{\lambda} = (C_g \sin\theta + \mathbf{U}/\text{east})(R \cos\phi)^{-1} \quad (4b)$$

$$\dot{\theta} = C_g \sin\theta \tan\phi R^{-1} + (\mathbf{k} \times \mathbf{k})k^{-2} \quad (4c)$$

$$\dot{\sigma} = \partial\sigma/\partial t \quad (4d)$$

where C_g is the group velocity, θ is the wave direction measured clockwise relative to true north, \mathbf{U} is the current velocity vector, \mathbf{k} is the wave number vector and $k=|\mathbf{k}|$ is the wavenumber. In Eqs. (4a) and (4b), “north” and “east” represent Latitude and Longitude of the earth, respectively. Eq. (2) is the basic transport equation which will be used in the wave prediction model.

The boundary conditions in SWAN, both in the geographic space and the spectral space, are fully absorbing boundaries. The wave energy is set to leave the computational domain or cross a coastal line. For coastal regions the incoming wave energy is only provided along the deepwater boundary. The spectral densities are assumed to be zero along the lateral boundaries. To avoid the propagation of numerical errors into the computational domain, the lateral boundaries are placed sufficiently far away from the area of interest.

3. The numerical schemes

3.1. The fractional step method

In SWAN, the numerical solution of the propagation of waves in both geographic and spectral spaces was described with a large basic matrix that needs to be solved iteratively until some convergence criteria

are met. The action balance equation in SWAN is solved by finite-difference scheme in all five dimensions. Time is discretized with a simple time-step for the propagation and source terms. The numerical propagation schemes for both geographic and spectral spaces in SWAN are implicit upwind schemes. Combining refraction, frequency shifting, and non-linear source terms from this basic matrix leads to a complicated matrix solution, in which the matrix is decomposed into four sections, which are solved in one step. When refined grids are used on small-scale regions, the basic matrix becomes large and requires a large memory storage and computational time.

An implicit approach in the multidimensional problem like SWAN requires solving multidimensional implicit equations. This rather formidable task can be circumvented by the application of the split method (Yanenko, 1971). Splitting the wave action balance equation into the geographic and spectral dimensions allows us to construct efficient numerical schemes with one-dimensional algorithms. The strong stability properties of the split method permit us to study the physical features of the equations, because the coefficients for diffusion may be changed over wide ranges without violating stability conditions. Eq. (1) is split into three space equations using three fractional steps on one time-step Δt as follows:

$$\frac{N^{n+1/3} - N^n}{\Delta t} + \frac{\partial}{\partial \sigma} (C_\sigma N) = 0 \quad (5)$$

$$\frac{N^{n+2/3} - N^{n+1/3}}{\Delta t} + \frac{\partial}{\partial \theta} (C_\theta N) = 0 \quad (6)$$

$$\frac{N^{n+1} - N^{n+2/3}}{\Delta t} + \frac{\partial}{\partial x} (C_x N) + \frac{\partial}{\partial y} (C_y N) = S_{\text{total}} \quad (7)$$

in which N^n , $N^{n+1/3}$, $N^{n+2/3}$, and N^{n+1} denotes the wave action density at time interval n , $n+1/3$, $n+2/3$, and $n+1$, respectively. Eq. (5) represents the action balance equation in the frequency space and is solved by the flux corrected transport method (Boris and Book, 1973). Eq. (6) represents the wave propagation in the directional space and is solved by the Crank–Nicolson method. Eq. (7) represents the wave propagation in the geographical space and is solved by the Finite Element Method.

3.2. Wave propagation in the frequency space

The integration of the action balance equation has been implemented in SWAN with a finite-difference scheme in five dimensions (the time, the geographic space, and the spectral space). The implicit finite-difference technique is endowed in the model with certain desirable features such as stability and exact conservation. In regions where large gradients of the action density in the frequency space are present, the truncation errors may become as large as the solution and numerical oscillations may arise, resulting in the negative values of the action density. For SWAN, in each sweep step, such negative values are set to be zero to ensure that the frequency-integrated action density per spectral direction is conserved.

To have better numerical stability, the Flux-Corrected Transport (FCT) algorithm (Boris and Book, 1973) is applied here to circumvent the steep-gradient problems by requiring the continuity and positivity of the action density. The algorithm consists of three major stages: the low-order transport stage, the anti-diffusion stage, and the corrected transport stage. These stages are all conservative and possess the positivity feature.

The finite-difference equations in the frequency space for calculating the flux F , by the first-order upwind scheme are given by

$$F_{j+1/2}^L = N_j \frac{C_{\sigma,j+1} + |C_{\sigma,j+1}|}{2} + N_{j+1} \frac{C_{\sigma,j+1} - |C_{\sigma,j+1}|}{2} \quad (8)$$

$$F_{j-1/2}^L = N_{j-1} \frac{C_{\sigma,j} + |C_{\sigma,j}|}{2} + N_j \frac{C_{\sigma,j} - |C_{\sigma,j}|}{2} \quad (9)$$

$$N_j^L = N_j^n - \frac{\Delta t}{\Delta \sigma} (F_{j+1/2}^L - F_{j-1/2}^L) \quad (10)$$

where N_j^L represents the action density at the low-order transport stage.

The central difference schemes employed to compute the flux at the high-order transport stage are

$$F_{j-1/2}^H = \frac{C_{\sigma,j-1} + C_{\sigma,j}}{2} N_j \quad (11)$$

$$F_{j+1/2}^H = \frac{C_{\sigma,j+1} + C_{\sigma,j}}{2} N_{j+1} \quad (12)$$

and the explicit anti-diffusion equations are written as

$$A_{j-1/2} = F_{j-1/2}^H - F_{j-1/2}^L \quad (13)$$

$$A_{j+1/2} = F_{j+1/2}^H - F_{j+1/2}^L \quad (14)$$

where $A_{j+1/2}$ and $A_{j-1/2}$ are the correcting action densities at the grid points $j-1/2$ and $j+1/2$, respectively. The corrected terms $A_{j+1/2}^L$ are given by the formula

$$\begin{aligned} A_{j+1/2}^L = & \operatorname{sgn}(A_{j+1/2}) \max \left\{ 0, \min \left[|A_{j+1/2}|, \operatorname{sgn}(A_{j+1/2}) \right. \right. \\ & \times \left(N_{j+2}^L - N_{j+1}^L \right) \Delta \sigma / \Delta t, \operatorname{sgn}(A_{j+1/2}) \\ & \left. \left. \times \left(N_j^L - N_{j-1}^L \right) \Delta \sigma / \Delta t \right] \right\} \end{aligned} \quad (15)$$

where

$$\operatorname{sgn}(A_{j+1/2}) = \begin{cases} 1, & \text{if } A_{j+1/2} \geq 0 \\ -1, & \text{if } A_{j+1/2} < 0 \end{cases} \quad (16)$$

and replace the $A_{j-1/2}$ by the corrected terms $A_{j-1/2}^L$. By means of a few tests, Boris and Book (1973) demonstrated that Eq. (15) is the quantitative form of the qualitative prescription. Using the corrected transport term to correct the low-order transport, the solution can be written as

$$N_j^{n+1/3} = N_j^L - \frac{\Delta t}{\Delta \sigma} \left(A_{j+1/2}^L - A_{j-1/2}^L \right) \quad (17)$$

where $N_j^{n+1/3}$ is the temporal result of the wave action density in the frequency space.

3.3. Wave propagation in the directional space

The numerical scheme in the wave propagation in the directional space is an implicit scheme that is economical with unconditional stability. It allows a larger time-step in the computation than that for the explicit scheme in shallow water. A second-order central approximation is supplemented in directional space and the discretization of Eq. (6) is thus given by

$$\begin{aligned} N_j^{n+2/3} = & N_j^{n+1/3} + \Theta \frac{\Delta t}{2\Delta \theta} \\ & \times \left[(C_\theta N)_{j-1}^{n+2/3} - (C_\theta N)_{j+1}^{n+2/3} \right] \\ & - (1 - \Theta) \frac{\Delta t}{2\Delta \theta} \left[(C_\theta N)_{j+1}^{n+1/3} - (C_\theta N)_{j-1}^{n+1/3} \right] \end{aligned} \quad (18)$$

where Δt and $\Delta \theta$ are the time and the directional step, respectively. Θ is the weighting factor ranging from 0 to 1. It has been shown that Eq. (18) is unconditionally stable as $\Theta \geq 1/2$. The value of Θ is chosen as $\Theta = 1/2$ in the present model.

3.4. Wave propagation in the geographic space

For convenience, Eq. (7) is written in a tensor form

$$\frac{N^{n+1} - N^{n+2/3}}{\Delta t} + \frac{\partial}{\partial x_i} (C_i N) = S_{\text{total}} \quad (19)$$

where the subscript $i=1, 2$ denotes x and y space, respectively. The action density N^{n+1} in Eq. (19) is expanded to the second-order approximation with respect to time using Taylor expansion, that is

$$\begin{aligned} N^{n+1} = & N^{n+2/3} + \Delta t \left. \frac{\partial N}{\partial t} \right|_{t=n+2/3} \\ & + \frac{\Delta t^2}{2} \left. \frac{\partial^2 N}{\partial t^2} \right|_{t=(n+2/3)+\Theta} \end{aligned} \quad (20)$$

in which

$$\left. \frac{\partial N}{\partial t} \right|_{t=n+2/3} = - \left[\frac{\partial}{\partial x_i} (C_i N) - S_{\text{total}} \right]_{t=n+2/3} \quad (21)$$

$$\begin{aligned} \left. \frac{\partial^2 N}{\partial t^2} \right|_{t=(n+2/3)+\Theta} = & - \frac{\partial}{\partial x_i} \left\{ C_i \left[\frac{\partial}{\partial x_j} (C_j N) - S_{\text{total}} \right] \right\}_{t=(n+2/3)+\Theta} \\ & - \frac{\partial S_{\text{total}}}{\partial N} \left[\frac{\partial}{\partial x_i} (C_i N) - S_{\text{total}} \right]_{t=(n+2/3)+\Theta} \end{aligned} \quad (22)$$

Substitution of Eqs. (21) and (22) into Eq. (20) results in the following discretized equation:

$$\begin{aligned} N^{n+1} = & N^{n+2/3} - \Delta t \left[\frac{\partial}{\partial x_i} (C_i N) - S_{\text{total}} \right]_{n+2/3} \\ & + \frac{\Delta t^2}{2} \left\{ \frac{\partial}{\partial x_i} \left[C_i \left(\frac{\partial (C_j N)}{\partial x_j} - S_{\text{total}} \right) \right] - \frac{\partial S_{\text{total}}}{\partial N} \right. \\ & \left. \times \left[\frac{\partial}{\partial x_i} (C_i N) - S_{\text{total}} \right] \right\}_{n+2/3} (1 - \Theta) \\ & + \frac{\Delta t^2}{2} \left\{ \frac{\partial}{\partial x_i} \left[C_i \left(\frac{\partial (C_j N)}{\partial x_j} - S_{\text{total}} \right) \right] - \frac{\partial S_{\text{total}}}{\partial N} \right. \\ & \left. \times \left[\frac{\partial}{\partial x_i} (C_i N) - S_{\text{total}} \right] \right\}_{n+1} \Theta \end{aligned} \quad (23)$$

The FEM with unstructured grids has the superiority of programming simplicity and thus is widely used in numerical models of large-scale oceanographic or coastal problems (e.g., Ou et al., 2002b). The boundary value problem described above is solved by the Taylor–Galerkin Finite Element Method of Donea (1984) and Selmin et al. (1985). Applying a weighted residual procedure, the action balance equation of Eq. (23) can be expressed as

$$\begin{aligned}
& \int_{\Omega} \zeta N^{n+1} d\Omega \\
&= \int_{\Omega} \zeta N^{n+2/3} d\Omega - \Delta t \\
&\quad \times \int_{\Omega} \zeta \left[\frac{\partial}{\partial x_i} (C_i N) - S_{\text{total}} \right]_{n+2/3} d\Omega \\
&\quad + (1 - \Theta) \frac{\Delta t^2}{2} \\
&\quad \times \int_{\Omega} \zeta \frac{\partial}{\partial x_i} \left[C_i \left(\frac{\partial}{\partial x_j} (C_j N) - S_{\text{total}} \right) \right]_{n+2/3} d\Omega \\
&\quad + \Theta \frac{\Delta t^2}{2} \int_{\Omega} \zeta \frac{\partial}{\partial x_i} \\
&\quad \times \left[C_i \left(\frac{\partial}{\partial x_j} (C_j N) - S_{\text{total}} \right) \right]_{n+1} d\Omega \quad (24)
\end{aligned}$$

where ζ is a weighting function. Notably, Eq. (24) contains domain integral in Ω and boundary integral on l . A linear shape function is required to describe the wave action density. Three-point triangular elements are used to discretize the computational domain. After some algebraic manipulation, the discretized form of Eq. (24) may be put as

$$\begin{aligned}
& \left[\mathbf{M} + \Theta \frac{\Delta t^2}{2} (\mathbf{VM}_b - \mathbf{SM}_b) \right] \mathbf{N}^{n+1} \\
&= \left[\mathbf{M} - \Delta t (\mathbf{VM}_a - \mathbf{SM}_a) - (1 - \Theta) \frac{\Delta t^2}{2} \right. \\
&\quad \left. \times (\mathbf{VM}_b - \mathbf{SM}_b) \right] \mathbf{N}^{n+2/3} \quad (25)
\end{aligned}$$

where the bold symbols denote matrices and are expressed as follows.

$$\mathbf{M} = \int_{\Omega} Z^T Z d\Omega \quad (26)$$

$$\mathbf{VM}_a = \int_{\Omega} Z^T Z_{,x_i} C_i d\Omega \quad (27)$$

$$\mathbf{VM}_b = \int_l (Z^T Z_{,x_j} C_i C_j) n_i dl - \int_{\Omega} Z^T_{,x_i} Z_{,x_j} C_i C_j d\Omega \quad (28)$$

$$\mathbf{SM}_a = \int_{\Omega} Z^T Z \psi^n d\Omega \quad (29)$$

$$\mathbf{SM}_b = \int_{\Omega} Z^T Z_{,x_i} \psi^n d\Omega \quad (30)$$

and

$$Z = [\zeta_1, \zeta_2, \zeta_3] \quad (31)$$

The superscript “ T ” denotes the transpose of a matrix. In Eqs. (29) and (30), there exist the source terms of wave energy generation and dissipation. To obtain a stable solution, the wave energy generation is discretized by an explicit method, whereas the energy dissipation is discretized by an implicit method, i.e.,

$$S_{\text{total}}^n = \psi^n N^n \quad (32)$$

$$\begin{aligned}
S_{\text{total}}^{n+1} &= \psi^n N^n + \frac{\partial S_{\text{total}}^n}{\partial N^n} (N^{n+1} - N^n) \\
&= \psi^n N^{n+1} \quad (33)
\end{aligned}$$

Notably, the numerical calculation in the present model is conducted in the spherical coordinates. We, therefore, have to transform the divergence and area elements into the spherical coordinates using the relations: $dx dy = R^2 \cos \phi d\lambda d\phi$, $\partial/\partial x = \partial/\partial \lambda (R \cos \phi)^{-1}$, and $\partial/\partial y = \partial/\partial \phi R^{-1}$. For reasons of computational economy, the explicit approximation is also used for the formulation of the quadruplet wave–wave interactions. The weighting factor Θ in Eq. (25) is adopted by 1/2, and it can be regarded as the form of the Crank–Nicolson numerical scheme. The numerical propagation schemes in the present study are the implicit schemes as used in SWAN. The time-step is

chosen on the basis of robustness, accuracy, and economy. Generally, the time-step is chosen small enough to have the Courant number close to 1.

To suppress numerical instabilities, the total change of the action density per interaction at each discrete wave component is confined to a fraction of 10% based on the Phillips’ equilibrium level, and the limiting criterion is given by

$$|\Delta N(\sigma, \theta)_{\max}| = \frac{0.1}{2\pi\sigma} \frac{\alpha_{PM}\pi}{k^3 C_g} \quad (34)$$

where $\alpha_{PM}=0.0081$ is the Phillip’s constant for the Pierson and Moskowitz’s (1964) spectrum. To retain

the rapid decrease of wave energy near the shore due to depth-induced wave breaking, the limitation is not applied if the waves actually break as used in SWAN.

For depth-induced wave breaking a spectral model of Battjes and Janssen (1978) is used in the present model. The breaking criterion is determined by $H_{\max}=\gamma' h$, in which γ' is the breaker parameter and it is often a constant or is expressed as a function of the Iribarren number (e.g., Galvin, 1972). An average value of $\gamma'=0.73$ is used in SWAN and FEM for the different types of bathymetry.

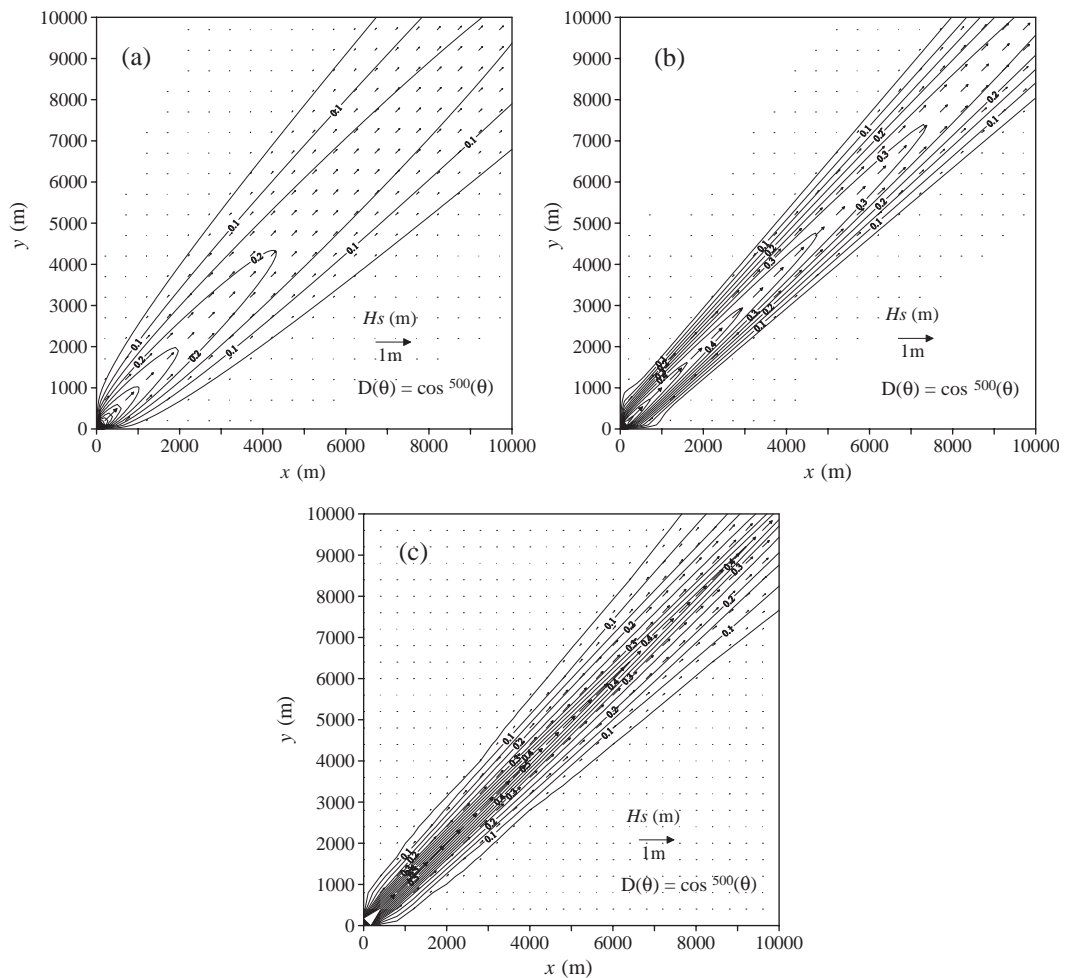


Fig. 1. Numerical diffusion in geographical space. (a) The propagation scheme with first-order (stationary case) backward space-backward time (BSBT) scheme; (b) the propagation scheme (stationary case) in SWAN model using second-order upwind scheme, SORDUP (Rogers et al., 2002); (c) the propagation scheme in the present model with second-order Taylor–Galerkin finite element scheme (Donea, 1984).

3.5. The input conditions

The input spectrum in the present model is discretized with a constant directional resolution $\Delta\theta$ and a constant relative frequency resolution $\Delta\sigma/\sigma$ with a logarithmic frequency distribution. Only wave components traveling in predefined directional sectors are used in the calculation. To save computer time, the discrete frequencies are specified between a fixed low cutoff frequency f_{\min} and a high cutoff frequency f_{\max} . Typically, $f_{\min}=0.04$ Hz and $f_{\max}=1$ Hz are used in the FEM model, as in WAM and SWAN. Above the high cutoff frequency, a diagnostic f^{-m} tail is added. According to Phillips (1985), the value of m is taken as 4.

For the sake of the iterative convergence and computational efficiency, the JONSWAP spectrum is chosen as the initial condition in the test of the model. The JONSWAP spectrum is given by Hasselmann et al. (1973)

$$E(f) = \alpha g^2 (2\pi)^{-4} f^{-5} \exp \left[-\frac{5}{4} \left(\frac{f_p}{f} \right)^4 \right] \times \gamma \exp \left[-(f-f_p)^2 / (2\sigma^2 f_p^2) \right] \tag{35}$$

where

$$\sigma = \begin{cases} 0.07, & f \leq f_p \\ 0.09, & f > f_p \end{cases} \tag{36}$$

$$\alpha = 0.076 X^{*-0.22} \tag{37}$$

$$f_p = 3.5(g/U_{10})X^{*-0.33} \tag{38}$$

where f_p is the peak frequency, $X^*=gX/U_{10}^2$ a dimensionless fetch, g the gravitational acceleration, X the fetch, U_{10} the wind speed at the elevation of 10 m above the mean sea level, and γ the peak enhancement factor taken as 3.3.

The directional distribution of Mitsuyasu (1975) is adopted to simulate the directional wave spectrum in the computation is given by;

$$G(\sigma, \theta) = G_0 \cos^{2s} \left(\frac{\theta - \theta_0}{2} \right) \tag{39}$$

where

$$G_0 = \frac{1}{\pi} 2^{2s-1} \frac{\Gamma^2(s+1)}{\Gamma(2s+1)} \tag{40}$$

θ_0 is the prevailing direction of wind waves, s is a parameter representing the degree of the directional energy concentration. In this study, s is set to be 10 and thus G_0 becomes 0.9.

4. Model validation

To verify the diffusion of the propagation scheme, the FEM model is used in simulating the stationary mode for a harmonic, long-crested wave propagating in deep water (computational area=10000 m×10000 m) through a gap at an angle of 45° with the positive x axis. The wave height in the gap is 1 m, and the frequency is 0.1 Hz. This harmonic wave is simulated with a Gaussian-shaped frequency spectrum with peak frequency 0.1 Hz, standard deviation 0.01 Hz, and a resolution of 3% of the frequency. The long crest in this case is simulated with a $\cos^{500} \theta$ directional distribution. The resolutions Δx and Δy are both 100 m and the directional resolution is 0.5° in all tests. Fig. 1 presents a comparison of numerical diffusion in the geographical space without source terms, as obtained by using the first order Backward-Space-Backward-Time (BSBT) scheme and the second-order upwind (SORLUP) scheme (Rogers et al., 2002) in the SWAN model, and the second-order Taylor–Galerkin finite element scheme (Donea, 1984) in the FEM model. In the figure, vectors represent the mean direction and magnitude of energy transport, and spreading of wave field is expressed as the width of the spatial distribution in the y direction. It is

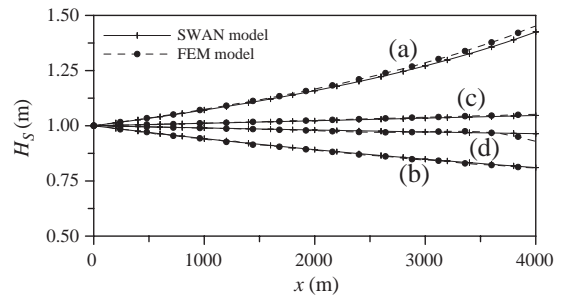


Fig. 2. Current-induced shoaling and refraction for monochromatic, long-crested waves. Waves traveling (a) against the current; (b) in the direction of the current; (c) across a slanting current with incident wave direction $\theta_0=30^\circ$; and (d) across a slanting current with incident wave direction $\theta_0=-30^\circ$. Circles with broken lines represent the present model results.

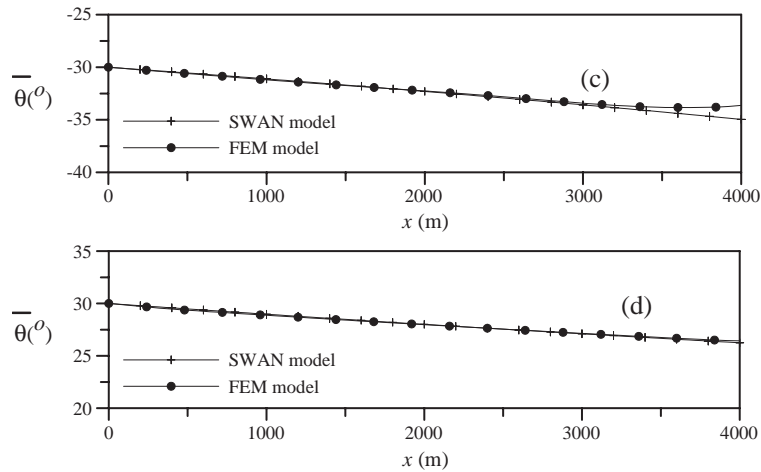


Fig. 3. Mean wave direction for the cases (c) and (d), as presented in Fig. 2.

important to note that good agreement of the diffusive spreading between the FEM model and the second order upwind scheme of SWAN is observed. It is readily apparent that a first-order scheme for the geographical diffusion propagation is the most serious type of numerical diffusion in SWAN.

In order to test the propagation scheme in the presence of an ambient current, we use the same wave propagating in deep water (from a uniform up-wave boundary over a distance of 4000 m) along the direction of current or in opposite current with speed U increased from 0 to 2 m/s in the down-wave direction. Comparisons of the simulated results in terms of a significant wave height by FEM and SWAN codes are shown as (a) and (b) cases in Fig. 2. Furthermore, current-induced refraction in deep water is tested by turning all of the ambient current direction

over 90° in the current field and the incident waves over 30° (positive or negative). The results obtained from FEM and SWAN computations are shown as (c) and (d) cases in Fig. 2. Notably, for all the four of these propagation tests with ambient currents, the agreement between these comparisons of the two models is again very good. The mean wave direction of the computational results is presented in Fig. 3. Interestingly, the FEM and SWAN results remain very similar except when the distance is larger than 3000 m in the x direction.

To test the propagation scheme in the shallow water with varying depth and without current, we consider the same waves (as used in the previous paragraph) propagating over a distance of 4000 m toward a plane beach with 20 m water depth and slope 1/200. In addition, the depth-induced refraction is added to it, by turning the incident wave direction over 30° . Figs.

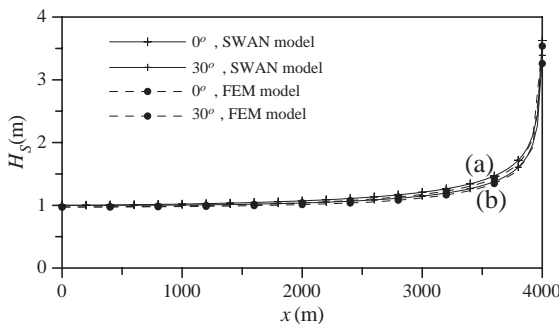


Fig. 4. Depth-induced shoaling and refraction for monochromatic, long-crested waves on a plane beach with slope 1/200. (a) Incident wave direction $\theta_0=0^\circ$; (b) incident wave direction $\theta_0=30^\circ$.

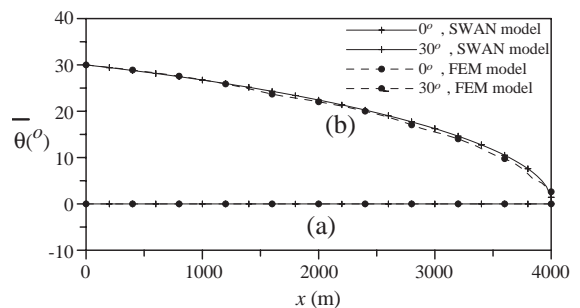


Fig. 5. Comparison of mean wave direction between the SWAN and the FEM codes in the shallow water with varying depth.

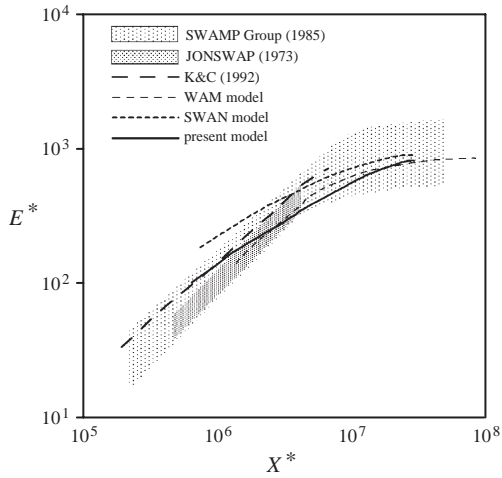


Fig. 6. Comparison of non-dimensional fetch-limited growth curves for the total energy E^* .

4 and 5 definitely show that the agreement is satisfactory between the FEM and SWAN results.

In order to check whether the FEM scheme has any negative impact on the source terms, further simulations are conducted that also helps us to make the necessary comparisons with the existing solution of Kahma and Calhoun (1992), JONSWAP (Hasselmann et al., 1974) and SWAMP Group (1985), and the limit values of WAM and SWAN models. A typical case of a constant wind blowing perpendicularly to a long and straight coastal line to generate waves is considered in the computation. The dimensionless total wave energy $E^* = g^2 E / U_*^4$ as a function of dimensionless fetch $x^* = gx / U_*^2$ is given in Fig. 6 for a stationary condition. The wind speed $U_{10} = 20$ m/s is taken to compute by WAM cycle 3, SWAN cycle III Version 40.31 and FEM models. It is interesting to note that the SWAN

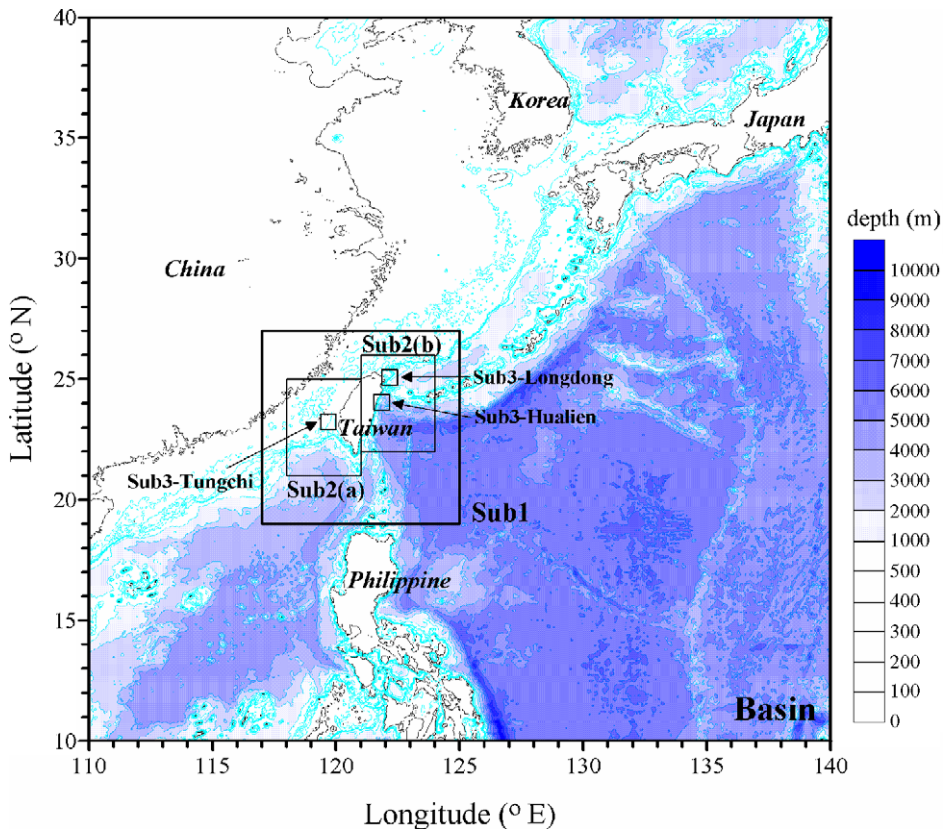


Fig. 7. The nested domain configuration of the SWAN model.

model overestimates the total energy as compared with the FEM results for the fetch area $x^* < 10^6$. The stationary growth curve (Fig. 6) as obtained by using the present FEM code falls midway between the previously published data. Such a comparison helps to convince that the FEM scheme for the propagation terms is not interacting negatively with the source terms.

5. Results and discussion

Wave hindcasting for both the monsoon and typhoon conditions are chosen here as the test cases for the present study. The selections are made for various combinations of high wind shear and storm activity, depending on the data availability.

The nested domain configuration and bathymetry are shown in Fig. 7. The bathymetry data for the Basin in SWAN were supplied by MEST V6.2 of NOAA variable grid bathymetry database (Smith and Sandwell, 1997). The spatial resolution of the database is approximately 3.6 km. The bathymetry database for the Sub1 (as defined below) and Sub2 (see Fig. 7) nests were obtained from National Center of Ocean Research, Taiwan (Liu et al., 1998). To obtain a more accurate bathymetry for the nearshore tested sites, the bathymetry for the Sub3 nest was taken from a hydrographic and land survey conducted by Taiwan Water Resource Agency, Taiwan. The bathymetry data in the FEM code were interpolated from the SWAN to fit the mesh node points. The location of buoy and wave stations for the tested areas are shown in Fig. 8.

In the SWAN code, as depicted in Fig. 7, four nests varying from coarse to fine resolution were used. The nests are referred to as the “Basin” (with 15-min interval and resolution of 121×121 grids), “Sub1” (with 5-min interval and resolution of 101×101 grids), “Sub2” (with 2.5-min interval and resolution of 76×101 grids), “Sub3” (with 0.6-min interval and resolution of 65×65 grids). The purpose of adding Sub2 and Sub3 is to obtain sufficient resolutions for the test site located near the shore.

The approximate mesh sizes are presented in Table 1. The length of the sides of the computational domain and the number of the grids in each wave direction were supplied in the SWAN code. The boundary condition of the spectra for Sub1 nest was taken from

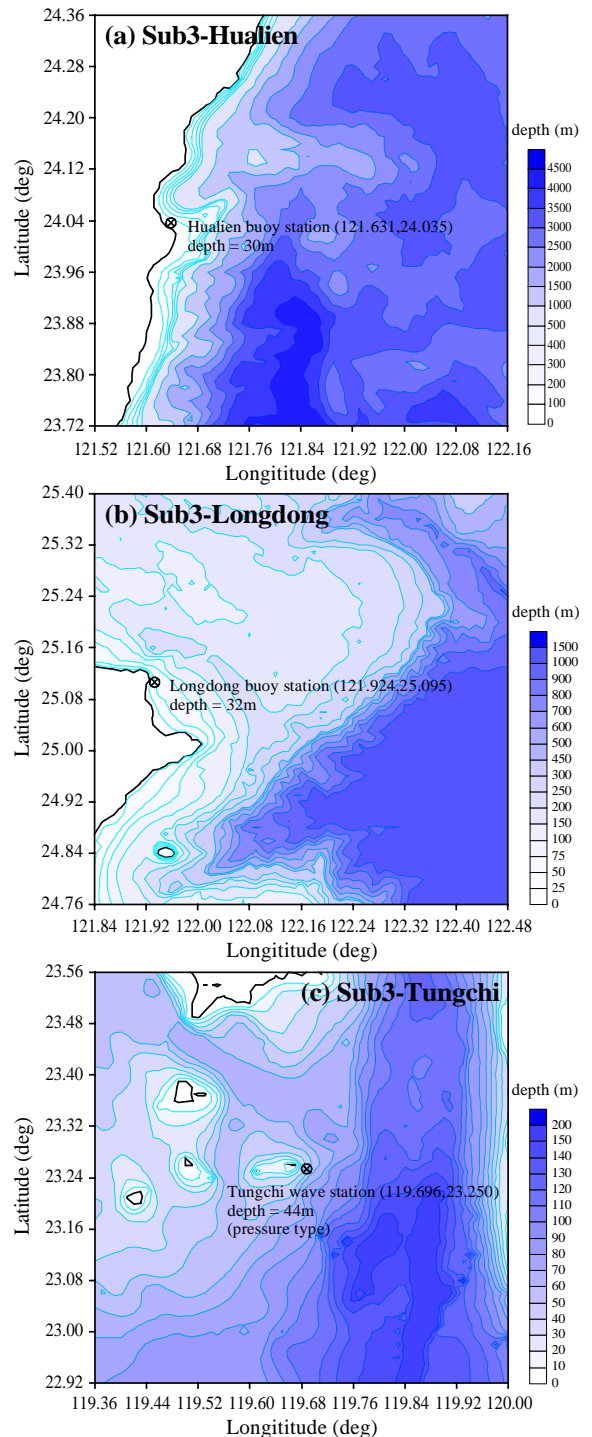


Fig. 8. The locations of wave and buoy stations for the test sites Sub3.

Table 1

Nest boundaries and mesh size

Nest regions	East long. (deg)	North lat. (deg)	Mesh size (km)
Basin	140/110	40/10	25
Sub1	125/117	27/19	8
Sub2-a	121/118	25/21	4
Sub2-b	124/121	26/22	4
Sub3-Hualien	122.16/121.52	24.36/23.72	1
Sub3-Longdong	122.48/121.84	25.40/24.76	1
Sub3-Tungchi	120.00/119.36	23.56/22.92	1

the computation on the Basin and that of Sub2 was obtained from Sub1, and for Sub3 it was provided by Sub2. The time-step for the Basin, Sub1, Sub2, and Sub3 are 30 min, 15 min, 10 min, 5 min, respectively. There were totally 25 exponential frequencies varying from 0.05 Hz to 1 Hz with 60 different directions used in the computation. The implementation of exponential frequency cut has the merit of higher resolution in lower frequency region and more efficient computation for the nonlinear wave–wave interaction.

For the computation of typhoon waves using the SWAN code, the nests, the mesh sizes, and the bathymetry database are kept the same as in the case of computation of monsoon waves. In the FEM code, the computational mesh consists of 3788 nodes and 7096 triangular elements as shown in Fig. 9. The coarsest meshes cover approximately 100 km on the

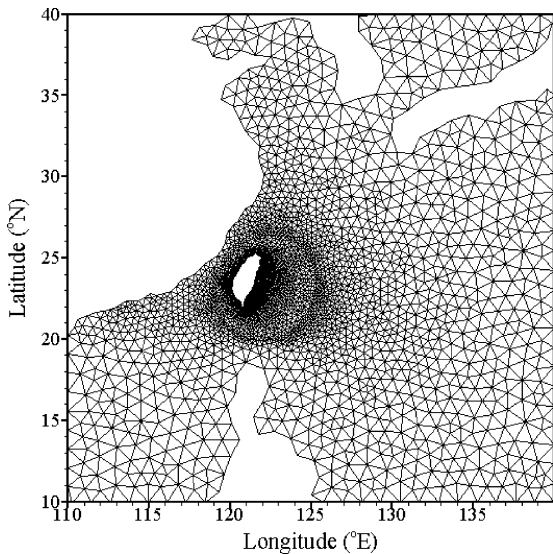


Fig. 9. The mesh configuration of the FEM code.

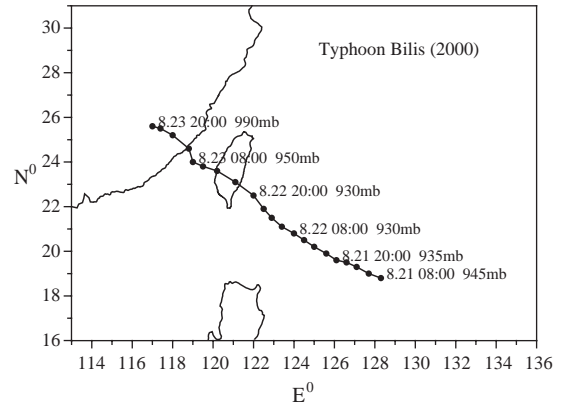


Fig. 10. The trajectory and central pressure of Typhoon Bilis provided by the Central Weather Bureau of Taiwan.

grid boundaries, whereas the most refined meshes cover less than 2 km near northeast coast of Taiwan.

Monsoon waves are normally generated by north-east wind fields during the winter season in Taiwan. The selected case of monsoon wave hindcasting is near Tungchi island which is located in southwest Taiwan strait, as shown in Fig. 7. There are a large number of wave observations available for verifications at the Tungchi station. The corresponding wind fields were derived from the atmospheric pressure, as supplied by the Central Weather Bureau (CWB) of Taiwan, using an aerodynamic model described by Ou et al. (2002b). The method is based on Ekman boundary layer dynamics which assume a balance between the pressure gradient, the Coriolis, and frictional forces in the atmospheric boundary layer (Yu, 1988). The wind observations from the wave station were used to check the model’s prediction ability. Waves were measured

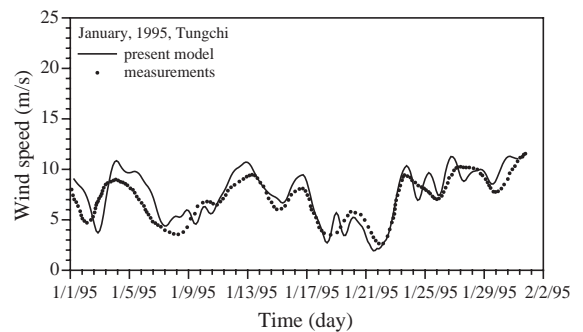


Fig. 11. Time series of wind speed at Tungchi station.

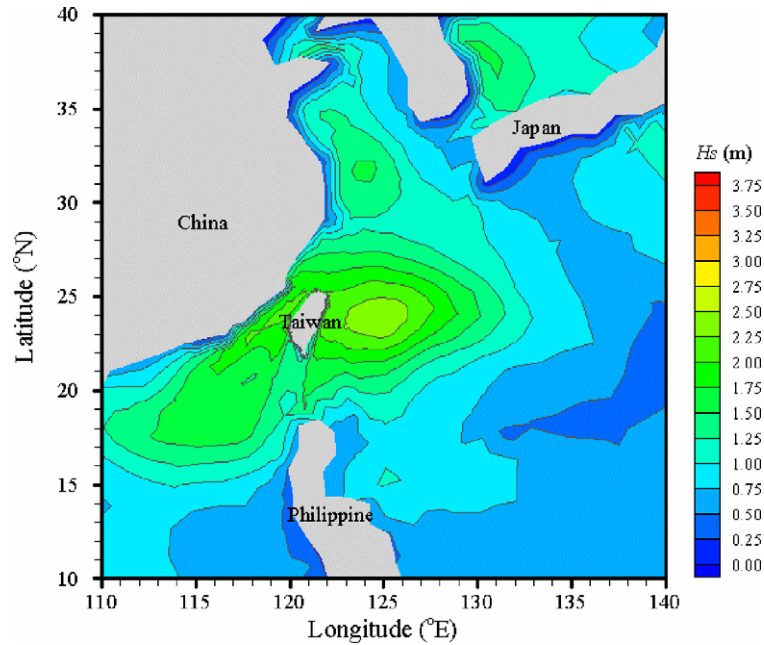


Fig. 12. FEM result for a significant wave height on January 13, 1995.

by a bottom-mounted pressure gauge. For each sub-nests, the wind fields are used as the input data in the SWAN code and the FEM code with some surface interpolation. The FEM and SWAN computations are compared with the wave data from the wave pressure gauge at Tungchi station. The wave pressure gauge is located 3 km offshore at a water depth of 44m as shown in Fig. 8c. The duration chosen for the computer simulation with FEM and SWAN runs is from January 1 to February 2, 1995, using a time-step of 5 min.

Typhoon Bilis hit the southeast coast of Taiwan during August, 2000 and it was one of the most violent typhoon. It left 15 people dead and caused 7.8 billion NT dollars in damage in the southeast of Taiwan. The path of Typhoon Bilis provided by CWB of Taiwan is shown in Fig. 10. At the center of the typhoon, the wind speed was 51 m/s during its impact with Taiwan island.

The typhoon wind fields used to run the FEM and the SWAN code computations were obtained using an

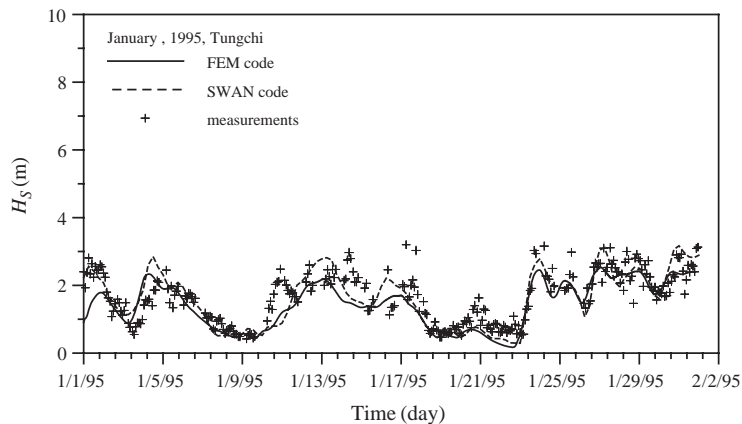


Fig. 13. Comparisons of significant wave heights between the predictions and the measurements at Tungchi station.

aerodynamic model (Ou et al., 2002b). The typhoon wind fields are first calculated on the Basin, which has a 15-min mesh interval and are interpolated to the subregion nests and node points using a bilinear surface interpolation method. Current and tidal effects were ignored in this study.

As shown in Fig. 8, the test sites Hualien and Longdong are located in the Pacific Ocean, along the northeast coast of Taiwan. The simulated results using the FEM and the SWAN codes were compared with the measured data from the two buoy stations Hualien (Fig. 8a) and Longdong (Fig. 8b). The water depth of the buoy is 30 m for the Hualien station and 32 m for the Longdong station.

The computational results from the FEM and the SWAN runs were evaluated using the correlation coefficient (CR) of Willmott (1981), as defined by

$$CR = \frac{\sum_{i=1}^N [(P_i - \bar{P})(O_i - \bar{O})]}{\left[\sum_{i=1}^N (P_i - \bar{P})^2 \sum_{i=1}^N (O_i - \bar{O})^2 \right]^{1/2}} \quad (41)$$

where P_i and O_i denote predicted and observed data, respectively, \bar{P} and \bar{O} are mean values of P_i and O_i , respectively, and N is the number of evaluation points.

Fig. 11 shows the comparison of the aerodynamic wind field model results for the computed wind speeds and measurements over 1 month for the Sub3 nest at the Tungchi station. It is noted that the predicted sea wind field is in relatively good agree-

Table 2

Comparisons of the hindcast procedure between the FEM and SWAN codes

Items code	FEM code	SWAN code
Number of grids or node points	3788	Basin (121×121) Sub1 (101×101) Sub2 (76×101) Sub3 (65×65)
Grid spacing	Max 100 km Min 2 km	Basin (25 km) Sub1 (8 km) Sub2 (4 km) Sub3 (1 km)
Computing time	38.37 h	Total 48.67 h Basin (4.62 h) Sub1 (5.88 h) Sub2 (6.5 h×2) Sub3 (8.39 h×3)
Correlation coefficients (CR)	Tungchi (CR=0.77) Hualien (CR=0.85) Longdong (CR=0.94)	Tungchi (CR=0.79) Hualien (CR=0.89) Longdong (CR=0.76)

ment with the observed data. The correlation coefficient CR is approximately 0.8.

Fig. 12 shows a typical example of the FEM result with significant wave height H_S in the Basin. The contour lines in the lower left of Fig. 12 are smooth, because the deep water depth does not play an important role of the evaluation of wave spectrum. As waves approach the nearshore zone, the iso-contour values began to show depth effects on wave braking and energy dissipation.

The pressure data from CWB with every three hours interval are used to interpolate the input wind

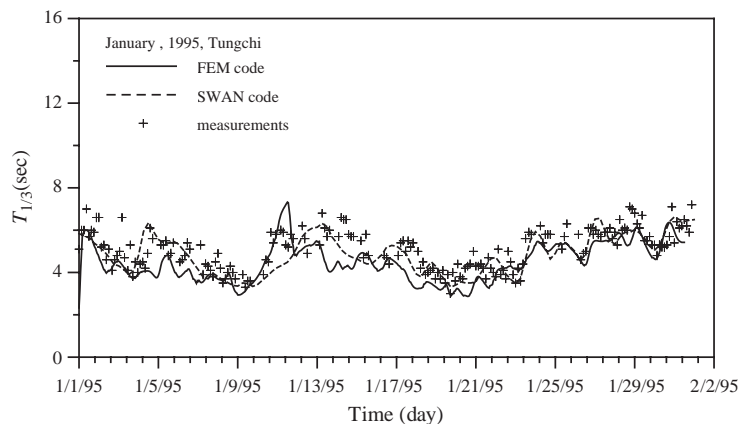


Fig. 14. Comparisons of the mean wave periods between the predictions and the measurements at Tungchi station.

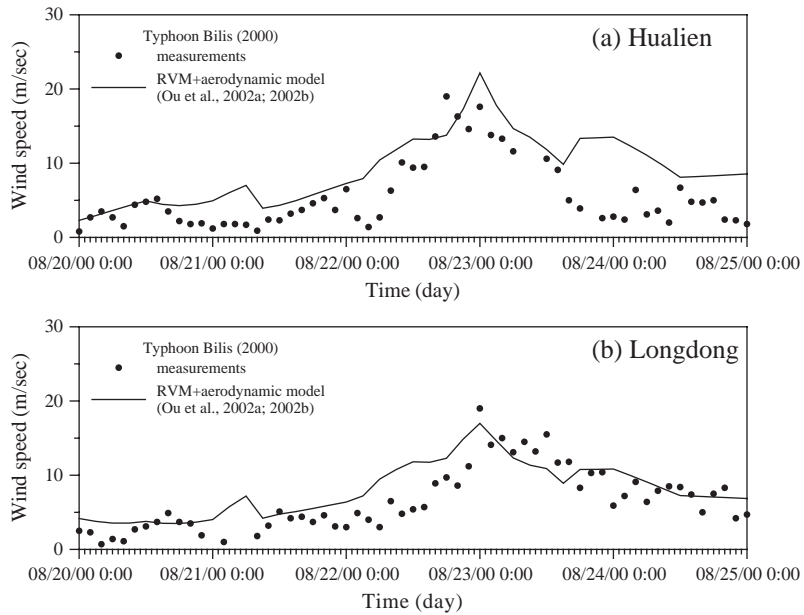


Fig. 15. Comparisons of the wind speeds between the present prediction and measurements during the passage of Typhoon Bilis.

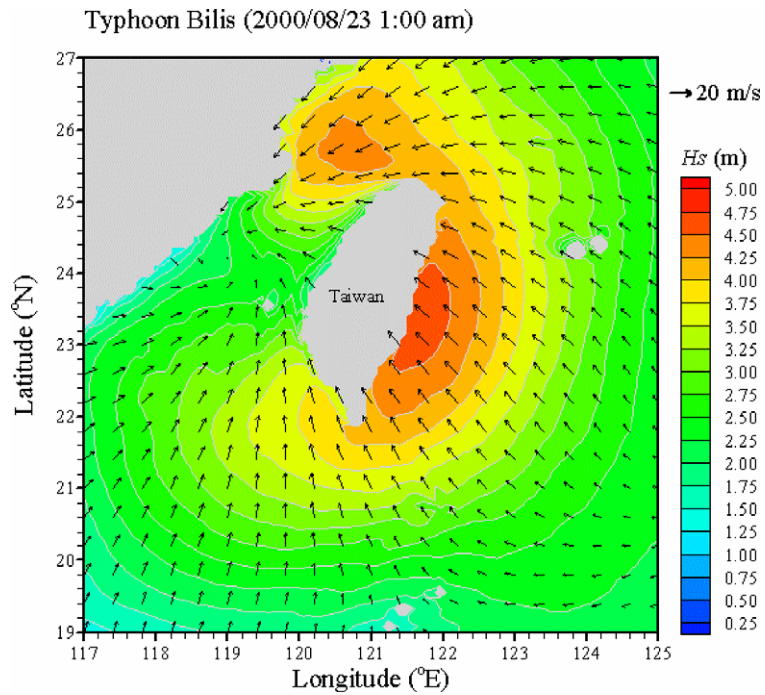


Fig. 16. Computed pattern of the significant wave height and mean wave direction around Taiwan coast on August 23 1:00 am, 2000.

fields and are too rough to exhibit the detailed rapid changes as the actual wind fields. Figs. 13 and 14 show the comparisons of the FEM and SWAN code results for the significant wave heights and the averaged wave periods. We notice that the FEM and SWAN results are quite similar, however, the predictions underestimate the peak values. Further comparisons between the predictions and measurements are evaluated by the correlation coefficients. At the Tungchi station, the correlation coefficients of wave height for the FEM and the SWAN code are $CR=0.77$ and 0.79 , respectively, as listed in Table 2.

For the simulation of typhoon waves, the Rankin Vortex Model (RVM) combined with the aerodynamic model developed by Ou et al. (2002a,b) was conveniently implemented to derive the wind fields for the wave models. The comparison of the wind speeds between the model results and measured data at Hualien and Longdong stations is presented in Fig.

15. The figure indicates that the wind fields are fairly predicted by the aerodynamic model.

The bathymetry and the mesh size for the typhoon waves computation are the same with those in the monsoon waves. To achieve more accurate nearshore wave conditions during the simulation period, the 10-min time-step was used for the FEM code, and the results agree well with real situations during rapid changes.

Fig. 16 demonstrates the pattern of a significant wave height and the mean wave direction as computed by the FEM code for August 23 1:00 am. The significant wave height reduces abruptly from the deepwater of 8 m to about 1 m in the nearshore zone. The comparisons between the computed and observed significant wave height and mean wave period at Hualien and Longdong stations are presented in Figs. 17 and 18. For the FEM model the agreement is generally reasonable. The SWAN model tends to

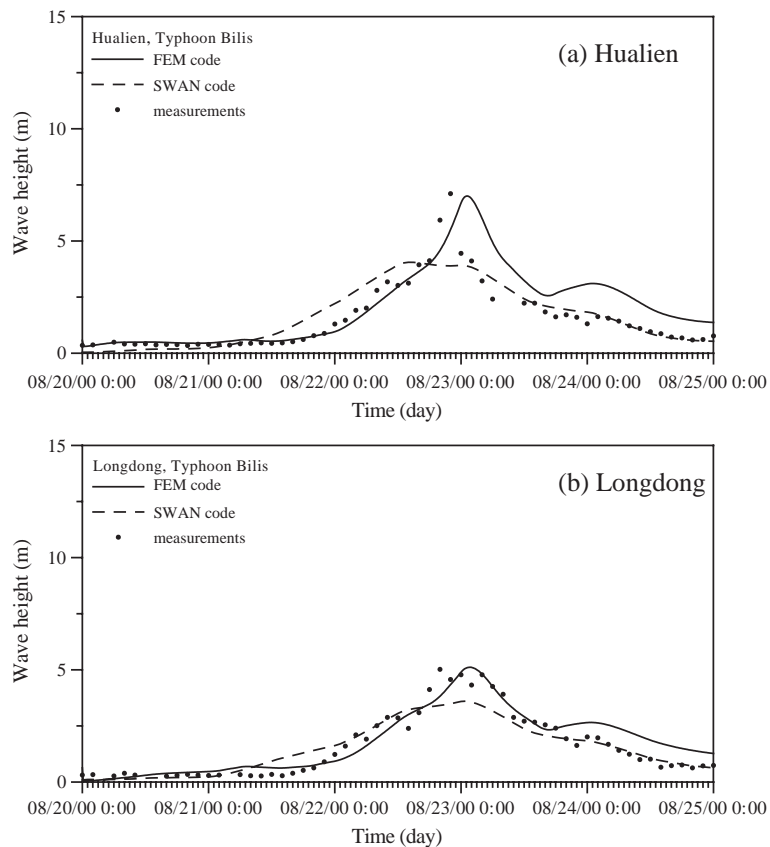


Fig. 17. A comparison between computed and observed significant wave height.

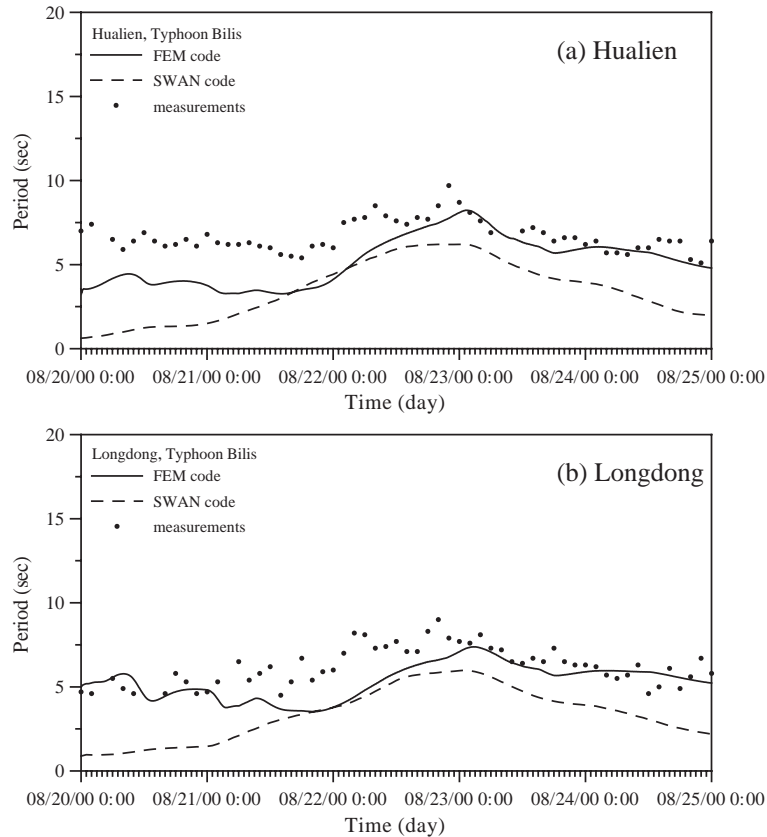


Fig. 18. A comparison between computed and observed mean wave period.

underestimate the peak values of the significant wave height and the mean wave period. The simulation for the subsequent rapid decrease in the wave height in front of the shore, as performed by the FEM, is better than that of SWAN, which is mainly caused by depth-induced breaking.

The FEM code has been developed for more efficient wave predictions in complicated bathymetries. It reduces the computing time for the nested grid system, because the local mesh size and number of nodes are optimized according to the desired resolution. The fractional step method was used to split the wave action balance equation into three one-dimensional space equations to simplify the complicated matrix solution in SWAN. The FCT scheme is applied in the FEM code to circumvent the steep-gradient problems in the frequency domain and to get a better numerical stability. The comparison of efficiency for both FEM and

SWAN models is given in Table 2. The computation is carried out by using Pentium 4, 3.06 GHz personal computer with 1 GB of memory, and Windows XP operation system. In the table, the number of nodes, grid spacing, computer time, and correlation coefficients are presented. Notably, the computing time is less with the FEM code, and it improves the spatial accuracy due to the fine mesh resolution in the nearshore region with implemented unstructured mesh.

6. Conclusions

The SWAN model is frequently used to simulate wave spectral transformations for both large-scale deep water oceans and small-scale shallow water domains. For real applications, the SWAN code usually needs additional finer nests to properly

represent bathymetric gradients and irregular boundaries. It requires a number of properties from the numerics of SWAN. For example, the size of the finite-difference spatial grid has to be decreased in each nest which highly increases the number of computational points. The numerical diffusion for wave propagation in SWAN will imply a strong decrease of the time-step in order to ensure that the Courant number remains a proper value to maintain numerical stability. Moreover, the computational procedures are laborious in coupling interface of nests through boundary spectra that were created by previous SWAN or WAM runs. This in turn implies a heavy management of input/output files, complicated programming, and the extra computer time, so that the computation does not become unrealistic at an operational stage.

Here a revised SWAN model using the Finite Element Method (FEM) was developed for wind wave simulation in both deep water oceans and shallow-water domains. The FEM has the merits to represent complex bathymetries and irregular shorelines accurately for a shallow water area and solve the large-scale oceanic and small-scale coastal problem in the same discrete domain using the unstructured meshes. The model employs a Taylor–Galerkin finite element technique for the proper resolution of bathymetric gradients and complicated boundaries. The computational area is discretized with a number of elements whose sizes are varied according to the desired resolution.

To enhance the computational efficiency, the fractional step method was implemented by splitting the governing equation into three one-dimensional space equations which avoids the huge matrix solution in SWAN and can be easily solved by one-dimensional algorithms. The Flux-Corrected Transport (FCT) was also applied to avoid the steep-gradient problems and to get a better stability in the calculations. Propagation tests with shoaling and refraction in deep and shallow water with and without currents show good agreement with results obtained from SWAN. A test of the energy growth curve convinces that the FEM scheme for the propagation terms do not interact negatively with the source terms.

The FEM and the SWAN codes were also applied for evaluations of model predictability on both monsoon and typhoon waves on the coastal waters of Taiwan using the wind and atmospheric pressure

data to derive the input energy. The computational results were compared with observations from wave pressure gauge and buoy stations. The numerical performance and efficiency of FEM and SWAN were examined through correlation coefficients. Comparisons of simulated wave heights and periods show that the numerical results obtained from the FEM model are in fairly good agreement with measurements. Furthermore, the FEM has the advantage to improve laborious procedures of the successive nested grids, which are time consuming for operation. The present model also matches the requirements of refined solution for the cases of complex bathymetries and irregular shorelines.

Acknowledgements

The National Science Council, Taiwan, is greatly appreciated for providing financial support for carrying out the research under the grant no. NSC93-2625-Z-006-005.

References

- Battjes, J.A., Janssen, P.A.E.M., 1978. Energy loss and set-up due to breaking of random waves. Proc. 16th Int. Conf. Coastal Engineering. ASCE, Hamburg, pp. 569–587.
- Booij, N., Ris, R.C., Holthuijsen, L.H., 1999. A third generation wave model for coastal regions: Part I. Model description and validation. J. Geophys. Res. 104, 7649–7666.
- Boris, J.P., Book, D.L., 1973. Flux corrected transport I, SHASTA, a fluid transport algorithm that works. J. Comp. Phys. 11, 38–69.
- Donea, J., 1984. A Taylor–Galerkin method for convective transport problem. Int. J. Numer. Methods Eng. 20, 101–119.
- Galvin Jr., C.J., 1972. Wave Breaking in Shallow Water. Waves on Beaches and Resulting Sediment Transport. Academic Press, Orlando, pp. 413–456.
- Hasselmann, K., Barnett, T.P., Bouws, E., Carlson, H., Cartwright, D.E., Enke, K., Ewing, J.A., Gienapp, H., Hasselmann, D.E., Kruseman, P., Meerburg, A., Müller, P., Olbers, D.J., Richter, K., Sell, W., Walden, H., 1973. Measurements of wind-wave growth and swell decay during the Joint North Sea Wave Project (JONSWAP). Dtsch. Hydrogr. Z., Suppl. 12, A8.
- Holthuijsen, L.H., Booij, N., Ris, R.C., Haagsma, I.J.G., Kieftenburg, A.T.M.M., Kriezi, E.E., Zijlema, M., 2000. SWAN Cycle III version 40.11 user manual.
- Kahma, K.K., Calkoen, C.J., 1992. Reconciling discrepancies in the observed growth of wind-generated waves. J. Phys. Oceanogr. 22, 1389–1405.

- Liu, C.S., Liu, S.Y., Lallemand, S.E., Lundberg, N., Reed, D., 1998. Digital elevation model offshore Taiwan and its tectonic implications. *Terr., Atmos. Ocean. Sci.*, TAO 9, 705–738.
- Mitsuyasu, H., 1975. Observations of the directional wave spectrum of ocean waves using a cloverleaf buoy. *J. Phys. Oceanogr.* 5, 750–760.
- Ou, S.H., Liao, J.M., Hsu, T.W., Tzang, S.Y., 2002a. Simulating typhoon waves by SWAN wave model in coastal waters of Taiwan. *Ocean Eng.* 29, 947–971.
- Ou, S.H., Hsu, T.W., Tzang, S.Y., Liao, J.M., 2002b. Wind wave hindcasting by a revised SWAN model using Finite Element Method. *Proc. of 1st German–Chinese Joint Symposium on Coastal and Ocean Engineering*, Rostock, Germany, pp. 167–185.
- Phillips, O.M., 1985. Spectral and statistical properties of the equilibrium range in wind-generated gravity waves. *J. Fluid Mech.* 156, 505–531.
- Pierson, W.J., Moskowitz, L., 1964. A proposed spectral form for fully developed wind seas based on the similarity theory of S.A. Kitaigorodskii. *J. Geophys. Res.* 69, 5181–5190.
- Rogers, W.E., Kaihatu, J.M., Petit, H.A.H., Booij, N., Holthuijsen, L.H., 2002. Diffusion reduction in an arbitrary scale third generation wind wave model. *Ocean Eng.* 29, 1357–1390.
- Selmin, V., Donea, J., Quartapelle, L., 1985. Finite Element Methods for nonlinear advection. *Comp. Meth. Appl. Mech. Eng.* 52, 817–845.
- Smith, W., Sandwell, D., 1997. Measurement and estimated seafloor topography. *World Data Center-A for Marine Geology and Geophysics Research Publication RP-1, Announcement 97-MGG-03*.
- SWAMP Group, 1985. *Ocean Wave Modeling*. Plenum Press, New York. 225 pp.
- WAMDI Group, 1988. The WAM model—a third generation ocean wave prediction model. *J. Phys. Oceanogr.* 18, 1775–1810.
- Willmott, C.J., 1981. On the validation of methods. *Phys. Geograp. J.* 2, 184–194.
- Wornom, S.F., Welsh, D.J.S., Bedford, K.W., 2001. On coupling of the SWAN and WAM wave models for accurate nearshore wave predictions. *Coast. Eng.* 43, 161–201.
- Yanenko, N.N., 1971. *The Method of Fractional Steps*. Springer-Verlag.
- Yu, T.S., 1988. A method for determining equivalent depths of the atmospheric boundary layer over the oceans. *J. Geophys. Res.* 93, 3655–3661.